Supporting Information

Soft X-ray Absorption Spectroscopy of Metalloproteins and High-Valent Metal-Complexes at Room Temperature Using Free-Electron Lasers

Markus Kubin[a], Jan Kern[b,c], Sheraz Gul[b], Thomas Kroll[d], Ruchira Chatterjee[b], Heike Löchel[e], Franklin D. Fuller[b], Raymond G. Sierra[c], Wilson Quevedo[a], Christian Weniger[a], Jens Rehanek[e,1], Anatoly Firsov[e], Hartawan Laksmono[f], Clemens Weninger[f,c], Roberto Alonso-Mori[c], Dennis L. Nordlund[d], Benedikt Lassalle-Kaiser[g], James M. Glownia[c], Jacek Krzywinski[c], Stefan Moeller[c], Joshua J. Turner[c], Michael P. Minitti[c], Georgi L. Dakovski[c], Sergey Koroidov[f,h], Anurag Kawde[h], Jacob S. Kanady[i], Emily Y. Tsui[i], Sandy Suseno[i], Zhiji Han[i], Ethan Hill[j], Taketo Taguchi[j], Andrew S. Borovik[j], Theodor Agapie[i], Johannes Messinger[h,k], Alexei Erko[e], Alexander Föhlisch[a,l], Uwe Bergmann[f,2], Rolf Mitzner[a], Vittal K. Yachandra[b,*], Junko Yano[b,*], Philippe Wernet[a,*]

[a]Institute for Methods and Instrumentation for Synchrotron Radiation Research, Helmholtz-Zentrum Berlin für Materialien und Energie GmbH, 12489 Berlin, Germany.

[b]Molecular Biophysics and Integrated Bioimaging Division, Lawrence Berkeley National Laboratory, Berkeley, CA 94720, USA.

[c]Linac Coherent Light Source, SLAC National Accelerator Laboratory, Menlo Park, CA 94025, USA.

[d]Stanford Synchrotron Radiation Lightsource, SLAC National Accelerator Laboratory, Menlo Park, CA 94025, USA.

[e] Institute for Nanometre Optics and Technology, Helmholtz-Zentrum Berlin für Materialien und Energie GmbH, 12489 Berlin, Germany.

[f] Stanford PULSE Institute, SLAC National Accelerator Laboratory, Menlo Park, CA 94025, USA.

[g] Synchrotron SOLEIL, L'Orme des Merisiers, Saint-Aubin, 91191 Gif-sur-Yvette, France.

[h] Institutionen för Kemi, Kemiskt Biologiskt Centrum, Umeå Universitet, SE 90187 Umeå, Sweden.

[i] Division of Chemistry and Chemical Engineering, California Institute of Technology, Pasadena, California 91125, USA.

[j] Department of Chemistry, University of California-Irvine, 1102 Natural Sciences II, Irvine, CA 92697-2025, USA.

[k] Department of Chemistry, Molecular Biomimetics, Ångström Laboratory, Uppsala University, SE 75237 Uppsala, Sweden.

[l] Institut für Physik und Astronomie, Universität Potsdam, 14476 Potsdam, Germany.

[1] Present address: Paul-Scherrer Institute, 5232 Villigen PSI, Switzerland.

[*] Authors to whom correspondence should be addressed.

Uwe Bergmann, Stanford PULSE Institute, SLAC National Accelerator Laboratory, Menlo Park, CA 94025, USA, Tel: 1 650 926 3048, email: bergmann@slac.stanford.edu; Vittal Yachandra, 1, Cyclotron Road, Lawrence Berkeley National Laboratory, Berkeley, CA, 94720, USA, Tel: 1 510 486 4963, vkyachandra@lbl.gov; Junko Yano, 1, Cyclotron Road, Lawrence Berkeley National Laboratory, Berkeley, CA, 94720, USA, Tel: 1 510 486 4366, jyano@lbl.gov; Philippe Wernet, Helmholtz-Zentrum Berlin, Albert-Einstein-Str. 15, 12489 Berlin, Germany, Tel: +49 30 806213448, email: wernet@helmholtz-berlin.de.

I. Sample Preparation

Recent spectroscopic studies have indicated that the multinuclear Mn complexes reported in ref. (34) of the main text are better assigned as one electron reduced oxo-hydroxo species instead of the previous assignment as dioxo species (ex: $Mn(III)_3CaO(OH)$ instead of $Mn(III)_2Mn(IV)CaO_2$), corresponding to the incorporation of one H-atom (Lionetti D, Suseno S, Tsui EY, Lu L, Carsch KM, Nielsen RJ, Goddard WA, Britt DR, Agapie T; Manuscript in preparation).

II. Reflection Zone Plate Spectrometer and Photon Count Rates

In the main text, we report a fluorescence-yield ratio of Mn $L_{\alpha,\beta}$: O $K_\alpha \approx 1 : 5400$ for the PS II S_1 (dark state) solution sample, averaged over the Mn L_3 resonance. With the following estimations we show that this is on the expected order of magnitude. Based on a Mn L-edge spectrum of a Mn^{2+}_{aq} solution with absolute absorption cross sections, as communicated by Schreck et al.[1] (see the peak absorption of $\sigma_{res}(\mathrm{Mn\ L_3}) \propto 12\ \mathrm{Mbarn}$, as used in the main paper) we estimate an *average* absorption cross section $\hat{\sigma}(\mathrm{Mn\ L_3})$ of Mn, averaged over the L_3 absorption edge, between 3 Mbarn (full foot-width) and 9 Mbarn (FWHM). Together with ref. (1) we thus estimate a ratio of x-ray absorption cross sections of $\hat{\sigma}(\mathrm{Mn\ L_3})/\sigma_O$ between 8 and 24 at ~640 eV photon energy. Including the relative fluorescence yield ratio $F_{MnL}/F_{OK} \sim 1/1.7$ (2), the relative diffraction efficiency of the zone plate optics for the Mn L and O K fluorescence yields, $R_{RZP}(637\ eV)/R_{RZP}(525\ eV) \approx 2$ (3), and the stoichiometric ratio of Mn:O ~ 1:64000 in the sample we expect a ratio of Mn $L_{\alpha,\beta}$: O K_α fluorescence photons between 1:2300 and 1:6800 for the PS II solution sample, which within the accuracy of these estimations agrees with the experimental ratio of 1:5400.

III. X-ray Pulse Energies at the Soft X-ray Instrument of the LCLS

The infrastructure of the soft x-ray instrument (SXR) of the Linac Coherent Light Source (LCLS) x-ray free-electron laser (XFEL) incorporates devices for measuring the pulse energy in at least two positons in the SXR beamline. In the beginning of the SXR beamline a device (here denoted as GMD1) monitors the x-ray induced luminescence in gases (4) and at the end of the SXR beamline a detection scheme for x-ray induced ion generation in gases (here named GMD2), measures the pulse energies (5-7) prior to refocusing of the pulsed beam towards the experiment. From the experimental values of these pulse energy monitors, GMD1 and GMD2, the energy of the x-ray pulses in the experimental interaction region can be estimated as done in ref. (22) of the main text.

If only GMD1 was available, measuring $E_p(\mathrm{GMD1})$ prior to entering the SXR beamline, the experimentally available pulse energy is estimated via

$$E_p = E_p(\mathrm{GMD1}) \cdot R^6 \cdot R_G \cdot \eta_{BW} \cdot c \qquad (1)$$

where R=0.79 is the assumed reflectivity of the mirrors and the KB optics, R_G is the reflectivity or diffraction efficiency of the monochromator grating with $R_G = 0.79$ in 0th order (reflection) or $R_G = 0.22$ in 1st diffraction order for the spectral range relevant to Mn L edge XAS. c=0.6 is a factor accounting for optical beam clipping in the beamline (ref. (22) of the main text). For the spectrum scans shown in the main text the full XFEL beam without further attenuation is used.

[1] Personal communication by S. Schreck and Ph. Wernet, Helmholtz-Zentrum Berlin, Germany 2017.

The fraction η_{BW} of photons transmitted on average by the monochromator is estimated as

$$\eta_{BW} = \frac{1}{2} \cdot \mathrm{erf}\left(\frac{\Delta E_{mono}/2}{\Delta E_{FEL}/(2\sqrt{2\ln(2)})/\sqrt{2}}\right) - \frac{1}{2} \cdot \mathrm{erf}\left(\frac{-\Delta E_{mono}/2}{\Delta E_{FEL}/(2\sqrt{2\ln(2)})/\sqrt{2}}\right) \quad (2)$$

with ΔE_{mono} being the bandwidth selected by the monochromator slit (typically 0.4 to 0.6 eV) and ΔE_{FEL} being the averaged bandwidth of the SASE spectrum, which was experimentally measured to be 4.2 eV at a photon energy of 640 eV, as shown in Fig. S1. $\mathrm{erf}(x)$ denotes the Gauss error function. For small ratios $\Delta E_{mono}/\Delta E_{FEL} \ll 1$ the approximation $\eta_{BW} \approx \Delta E_{mono}/\Delta E_{FEL}$ holds.

If the gas monitor detector GMD2 was available, measuring the pulse energy $E_p(\mathrm{GMD2})$ closer to the experiment, the pulse energy on the sample is estimated via

$$E_p = E_p(\mathrm{GMD2}) \cdot R^2 \quad (3)$$

where $R = 0.79$ is the nominal reflectivity of one KB optical element between GMD2 and the experimental chamber, as used for earlier estimations in ref. (22) of the main text. The ideal transmission of the combination of KB optics is thereby assumed to be $R^2 = 0.62$, which is on the order of the factor of around 0.5, given by Moeller et al. (7).

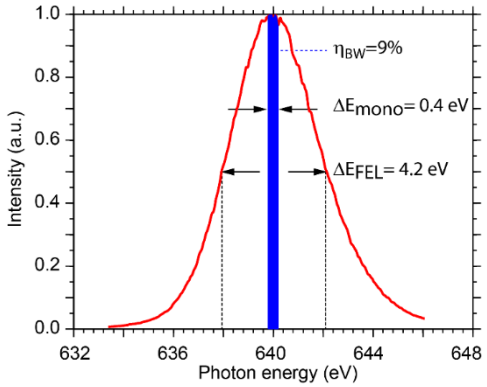

Fig. S1: An averaged LCLS SASE spectrum (integrated for ~10 s) with a bandwidth of 0.66% (FWHM) is shown in red. A typical bandwidth to be selected by the monochromator slit is sketched in blue. The spectrum was measured on a YAG screen placed in the beam diffracted by the monochromator grating in the 1st diffraction order.

Table S1: Determination of the pulse energy on the sample. We use the last two columns for further estimations.

Beamtime	Run #	Sample	ΔE_{mono} (eV)	GMD1 (mJ)	GMD2 (μJ)	E_p (μJ) from GMD 1	E_p (μJ) from GMD2	E_p (μJ) Aver-aged	N_p (ph/pulse) Averaged
LB68 (2013)	39	$Mn(II)Mn(III)_2CaO(OH)$	0.6	2.2	-	**9.4**	-	(9.4)	$(9.1 \cdot 10^{10})$
LK48 (2016)	83	Mn^{2+}_{aq}	0.4	1	10	2.8	6.3	**4.6**	$\mathbf{4.5 \cdot 10^{10}}$
LK48 (2016)	89	$Mn(III)_3CaO(OH)$	0.4	1	10	2.8	6.3	**4.6**	$\mathbf{4.5 \cdot 10^{10}}$
LK48 (2016)	87	$Mn(IV)_3CaO_4$	0.4	1	10	2.8	6.3	**4.6**	$\mathbf{4.5 \cdot 10^{10}}$
LK48 (2016)	104, 106	PS II (dark)	0.4	0.85	7	2.4	4.4	**3.4**	$\mathbf{3.3 \cdot 10^{10}}$
LK48 (2016)	121	PS II (2F)	0.4	0.85	9	2.4	5.6	**4.0**	$\mathbf{3.9 \cdot 10^{10}}$

Typical experimental pulse energies provided by the soft x-ray instrument SXR during the beamtimes LB68 (2013) and LK48 (2016) were calculated from experimental GMD1 and GMD2 values using equations (1)-(3) in Table S1. Apparently E_p(GMD2) yields ~50% higher pulse energies than E_p(GMD1) and is likely to overestimate the true pulse energy. In the main text the effective pulse energy on the sample is averaged from both values GMD1 and GMD2 (if available, i.e. for LK48).
In this case, the uncertainty of 25% assigned to all pulse energy measurements and therefrom deduced values reflects the discrepancy of the pulse energies estimated from the GMD2 and GMD1 values, respectively. For the beamtime LB68 (i.e. for the $Mn(II)Mn(III)_2CaO(OH)$ sample) the pulse energy is determined solely from GMD1 and is likely to be overestimated. From the averaged pulse energies E_p the number of photons per pulse on the sample N_p is calculated for a photon energy of $h\nu \approx 640$ eV $\approx 1.03 \times 10^{-10}$μJ using the equation

$$N_p = E_p / h\nu \tag{4}$$

The last two columns in Table S1 are used for all further estimations.

Furthermore, we assume the x-ray pulses to have a Gaussian distribution along the spatial axis of propagation, *z*, along the perpendicular axis pointing towards the spectrometer entrance, *x*, and along the perpendicular vertical axis, *y*. The pulse profile in the time domain *t*, thus, is also assumed to have a Gaussian distribution. The horizontal and vertical width (FWHM) of the pulse profile projected onto the x-y plane was measured for each experiment either from an in-situ luminescence profile on a YAG screen or with an offline fluence-scan imprint method on lead tungstenate (ref. (59) of the main text). The spatial photon (and energy) density profile and the intensity profile of the x-ray pulses on the sample as well as their peak and average values are estimated with the following set of equations.

The area density $n(x, y)$ of photons approximated by a two-dimensional Gaussian profile with a peak photon density n_0, horizontal width σ_x and vertical width σ_y is expressed as

$$n(x, y) = n_0 \cdot exp\left(-\left(\frac{x^2}{2\sigma_x^2} + \frac{y^2}{2\sigma_y^2}\right)\right) \tag{5}$$

where the Gaussian widths σ_i can be related to the FWHM values via $\sigma_i = FWHM_i/(2\sqrt{2\ln(2)})$.

The area density of photons per pulse is linked to the photon number N_p per pulse via

$$N_p = \int_{-\infty}^{+\infty}\int_{-\infty}^{+\infty} n(x,y)\,dxdy = \frac{\left(\sqrt{2\pi}\right)^2 n_0 \cdot FWHM_x \cdot FWHM_y}{\left(2\sqrt{2\ln(2)}\right)^2} \tag{6}$$

The peak value n_0 of the area density of photons for an average single pulse is calculated from the measured pulse energy E_p or the photon number N_p (see Table S1), respectively, and the widths $FWHM_x$, and $FWHM_y$ of the measured beam profile

$$n_0 = \frac{\left(2\sqrt{2\ln(2)}\right)^2 \cdot N_p}{\left(\sqrt{2\pi}\right)^2 \cdot FWHM_x \cdot FWHM_y} \tag{7}$$

The photon density $n(x,y)$ is linked to the energy fluence via $\epsilon(x,y) = h\nu \cdot n(x,y)$. Thus, the peak energy density of a pulse with $h\nu \approx 640$ eV $\approx 1.03 \times 10^{-16}$J is

$$\epsilon_0 = \frac{\left(2\sqrt{2\ln(2)}\right)^2 \cdot E_p}{\left(\sqrt{2\pi}\right)^2 \cdot FWHM_x \cdot FWHM_y} \tag{8}$$

The intensity distribution (energy density per time and area) of a Gaussian pulse is expressed as

$$I(x,y,t) = I_0 \cdot exp\left(-\left(\frac{x^2}{2\sigma_x^2} + \frac{y^2}{2\sigma_y^2} + \frac{t^2}{2\sigma_t^2}\right)\right) \tag{9}$$

With the peak intensity I_0 and the Gaussian width in time σ_t. It is linked to the energy fluence $\epsilon(x,y)$ by the integration over time. The integral for the peak value at $(\mathrm{x},\mathrm{y}) = (0,0)$ is

$$\epsilon_0 = \int_{-\infty}^{+\infty} \mathrm{I}(0,0,\mathrm{t})\,dt = I_0 \cdot \frac{\sqrt{2\pi} \cdot FWHM_t}{(2\sqrt{2\ln(2)})} \tag{10}$$

Thus, the peak intensity can be expressed in terms of the pulse energy and the pulse dimensions.

$$I_0 = \frac{\left(2\sqrt{2\ln(2)}\right)^3 \cdot E_p}{\left(\sqrt{2\pi}\right)^3 \cdot FWHM_t \cdot FWHM_x \cdot FWHM_y} \tag{11}$$

The peak values of the area density of photons and of energy and the peak intensity for the individual spectra shown in the main text are calculated from Table S1 and listed in Table S2.

In the presented PFY-XAS experiment the spatial photon density profile is averaged in several dimensions. In order to estimate the *effective* influence of x-ray beam damage to the sample an appropriate averaging factor needs to be considered. In a liquid jet sample environment of dilute samples exponential damping due to x-ray absorption by the solvent according to Beer-Lambert's law needs to be considered, which lead to a decreased Intensity along the x-ray beam axis z.

$$I(x,y,z_b) = I(x,y,0) \cdot \exp(-z_b/\Lambda) \tag{12}$$

Table S2: Peak values of the area density of photons (photon fluence) n_0, the energy fluence ϵ_0 and intensity I_0.

				Beam profile (exp.)		**Calculated peak values**		
Beamtime	Run #	Sample	τ_p(fs) (FWHM)	$FWHM_x$ (h) (µm)	$FWHM_y$ (v) (µm)	n_0 (ph/Å²)	ϵ_0 (J/ cm²)	I_0 (mJ/cm²/fs)
LB68 (2013)	39	$Mn(II)Mn(III)_2CaO(OH)$	200	20	140	0.29	0.30	1.4
LK48 (2016)	83	Mn^{2+}_{aq}	100	12	50	0.65	0.67	6.3
LK48 (2016)	89	$Mn(III)_3CaO(OH)$	100	12	60	0.55	0.56	5.2
LK48 (2016)	87	$Mn(IV)_3CaO_4$	100	12	60	0.55	0.56	5.2
LK48 (2016)	104, 106	PS II (dark)	100	10	50	0.58	0.60	5.6
LK48 (2016)	121	PS II (2F)	100	10	50	0.69	0.71	6.7

Λ is the attenuation length of the solution sample and z_b is the pathlength of the beam in the bulk of the solution sample.

An appropriate reference volume for estimating a generalized averaging factor for the probed sample volume is the "skin volume" $V_s = \pi \cdot \mathrm{FWHM_x} \cdot FWHM_y/4 \cdot \Lambda$ spanned by the attenuation length Λ of the sample and the elliptical area covered by the x-ray focus. This volume is defined in analogy to that used for calculating the "skin dose" (ref. (21) of the main text). This skin volume average is denoted by the subscript "s" in the averaged pulse parameters. One finds a generalized averaging factor γ_s such that

$$\bar{I}_s = \frac{1-1/e}{2\cdot\ln(2)} \cdot I_0 = \gamma_s \cdot I_0. \qquad (13)$$

In analogy, the averaging factor $\gamma_s = 0.456$ also applies for relating the average energy fluence $\bar{\epsilon}_s = \gamma_s \cdot \epsilon_0$ and the area density of photons $\bar{n}_s = \gamma_s \cdot n_0$ to the respective peak values. These skin volume averaged magnitudes are listed in Table 1 of the main text and are used for estimating the averaged, thus, effective influence of x-ray damage mechanisms.

This estimate for an averaging factor was compared to numerical simulations (not shown) which take into account the complete spatial geometry and exponential damping of the x-ray beam profile (for both incident and fluorescent photons) relative to the jet dimensions with geometry parameters close to those measured in the experiment. In fact, the averaging factors obtained from the simulation range between 60% and 100% of the skin-volume averaging factor $\gamma_s = 0.456$, thereby giving an upper limit character to the generalized averaging approach.

Table S3: Skin doses D_s calculated with eq. (14) for the experimental parameters.

Beamtime	Run #	Sample	E_p (µJ)	FWHM$_x$ (h) (µm)	FWHM$_y$ (v) (µm)	D_s (MGy)
LB68 (2013)	39	$Mn(II)Mn(III)_2CaO(OH)$	9.4	20	140	1.7[#]
LK48 (2016)	83	Mn^{2+}_{aq}	4.6	12	50	4.0
LK48 (2016)	89	$Mn(III)_3CaO(OH)$	4.6	12	60	3.2
LK48 (2016)	87	$Mn(IV)_3CaO_4$	4.6	12	60	3.2
LK48 (2016)	104, 106	PS II (dark)	3.4	10	50	3.4
LK48 (2016)	121	PS II (2F)	4.0	10	50	4.0

IV. X-ray Damage

IV.1 Dose Effects

Dose-dependent x-ray damage plays a major role for synchrotron-based studies of biological samples. For bulk samples with extensions larger than the attenuation length of the x-rays a typical magnitude considered in literature for characterizing the progress of sample damage is the "skin dose" D_s (ref. (21) of the main text), i.e. the energy absorbed within the skin volume (see previous section) divided by the mass of this volume. We calculate the skin dose via

$$D_s = \frac{E_p \cdot (1 - 1/\mathrm{e})/2}{\rho \cdot \Lambda \cdot \pi \cdot \mathrm{FWHM_x} \cdot FWHM_y/4} \tag{14}$$

Where the factor $(1 - 1/e)$ accounts for the fraction of photons absorbed within the attenuation length, the factor $1/2$ accounts for the photons contained in the elliptical area $\mathrm{A} = \pi \cdot \mathrm{FWHM_x} \cdot FWHM_y/4$ spanned by the horizontal and vertical focus size (FWHM). ρ is the mass density of the sample, here of the solvent with ρ~1 g/cm³. Λ is the attenuation length at 640 eV photon energy, which for aqueous solutions is approximated with the x-ray attenuation length $\Lambda = 0.80$ µm of liquid water at 640 eV photon energy using the CXRO data base[2] and ref. (1). The skin doses for the experiments shown in the main text are listed in Table S3.

IV.2 Sequential Multiphoton Absorption

In the presented experiment, sequential probing of the same sample volume by two independent x-ray pulses can be excluded due to continuous sample refreshment at a rate of >1 kHz, whereas the FEL repetition rate is 120 Hz. However, for XFEL sources sequential absorption of x-ray photons within a single x-ray pulse may occur with non-negligible probabilities and needs to be controlled. The probability for the (linear) absorption of an x-ray photon on the Mn L_3 resonance

$$p_{res} = n \cdot \sigma_{res} \tag{15}$$

is determined by the resonant (peak) absorption cross section of Mn which is on the order of[3]

$$\sigma_{res}(\mathrm{Mn\ L_3}) \propto 12\ \mathrm{Mbarn} = 6 \times 10^{-22}\ \mathrm{m^2}. \tag{16}$$

[2] http://henke.lbl.gov/optical_constants/

[3] Personal communication by S. Schreck and Ph. Wernet, Helmholtz-Zentrum Berlin, Germany 2017.

Table S4: Average (effective) probabilities for multiple Mn resonant L-edge absorption $\bar{P}^m_{MPA}$ for molecules with m Mn atoms. The probabilities are calculated using equations (15) to (18).

Beamtime	Run #	Sample	m	$\bar{n}_s$ (ph/Å²)	$\bar{p}_{res}$ (ph/Mn)	$\bar{P}^m_{MPA}$ (%)
LB68 (2013)	39	$Mn(II)Mn(III)_2CaO(OH)$	3	0.13	0.0079	2.4
LK48 (2016)	83	Mn^{2+}_{aq}	1	0.30	0.018	1.8
LK48 (2016)	89	$Mn(III)_3CaO(OH)$	3	0.25	0.015	4.4
LK48 (2016)	87	$Mn(IV)_3CaO_4$	3	0.25	0.015	4.4
LK48 (2016)	104, 106	PS II (dark)	4	0.27	0.016	6.3
LK48 (2016)	121	PS II (2F)	4	0.32	0.019	7.4

Upon absorption of one x-ray photon the 2p core hole state decays within ~2 fs, which is negligibly small as compared to the pulse duration of ~100 fs. Within this approximation, Poisson statistics can be used to estimate the probability $P(k) = (p_{res})^k/k! \cdot \exp(-p_{res})$ for an atom to resonantly absorb k photons ($k \geq 0$ being an integer number) within a single pulse. The probability that a photon, being resonantly absorbed by a single Mn atom, is not the first photon to be absorbed within the duration of the x-ray pulse can be expressed as a function of p_{res}:

$$P_{MPA} = \sum_{k=2}^{\infty} P(k) \Big/ \sum_{k=1}^{\infty} P(k) = \frac{1 - P(1) - P(0)}{1 - P(0)} = \frac{1 - \exp(-p_{res}) \cdot (1 + p_{res})}{1 - \exp(-p_{res})} \quad (17)$$

In the general case that a molecule contains m Mn atoms, the above equation can be generalized to calculate P^m_{MPA} (in the main text briefly P^m), being the fraction of photons which are absorbed by a molecule that has already absorbed another photon within the same x-ray pulse. Considering the total absorption cross section of all m Mn atoms in the molecule $p^m_{res} = p_{res} \cdot m$ the probability P^m reads

$$P^m = \frac{1 - \exp(-m \cdot p_{res}) \cdot (1 + m \cdot p_{res})}{1 - \exp(-m \cdot p_{res})} \quad (18)$$

Fig. S2 shows the fractions P^m plotted for molecules with m=1, m=3 and m=4 atoms as a function of p_{res}, the average number of photons absorbed on the Mn L_3 resonance. These cases resemble the estimates for multiple photon absorption for the Mn^{2+}_{aq} solution sample (m=1), the Mn_3CaO_x model compound samples (m=3) and the Mn_4CaO_5 cluster in a PS II sample (m=4). The skin-volume averaged values $\bar{P}^m$ estimated for the experimental conditions are listed in Table S4 and were calculated with the averaged area density of photons, $\bar{n}_s = \gamma_s n_0$.

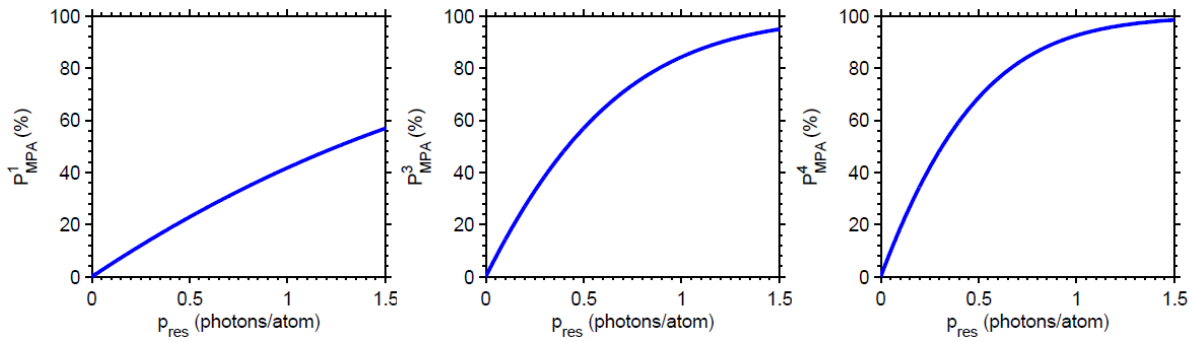

Fig. S2: Calculated fraction P^m_{MPA} of multiple photon absorption per pulse by a molecule with m=1 (left), m=3 (center) and m=4 (right) Mn atoms.

Table S5: The x-ray optical transparency of Mn atoms on the L_3 resonance due to (nonlinear) x-ray stimulated emission, as calculated using the formalism from ref. (51) of the main text. The intensities and transparencies are given for the most intense spot in the x-ray focus (peak) and averaged over the probed skin volume, respectively.

							peak intensity		skin volume average	
Beam-time	Run #	Sample	c(Mn) (mM)	E_p (μJ)	τ_p (fs)	Focus (HxV) (μm²)	I_0 (TW/cm²)	T_{NL} (%)	$\bar{I}_s$ (TW/cm²)	$\bar{T}_{NL}$ (%)
LB68 (2013)	39	$Mn(II)Mn(III)_2CaO(OH)$	15	9.4#	200	20x140	1.4	0.10	0.63#	0.048#
LK48 (2016)	83	Mn^{2+}_{aq}	500	4.6	100	12x50*	6.3	13	2.9	6.5
LK48 (2016)	89	$Mn(III)_3CaO(OH)$	10.5	4.6	100	12x60*	5.2	0.28	2.4	0.13
LK48 (2016)	87	$Mn(IV)_3CaO_4$	6	4.6	100	12x60*	5.2	0.16	2.4	0.072
LK48 (2016)	104, 106	PS II (dark)	0.8	3.4	100	10x50*	5.6	0.023	2.6	0.010
LK48 (2016)	121	PS II (2F)	0.8	4.0	100	10x50*	6.7	0.027	3.0	0.012

IV.3 Nonlinear X-ray Optical Effects and Stimulated Emission

Recent studies have demonstrated the potential for a decreased x-ray absorption signal due to stimulated forward scattering for high densities of soft x-ray photons (ref. (51) of the main text). These findings suggest a potential depletion of $2p \rightarrow 3d$ core excited Mn states at high x-ray intensities due to stimulated $3d \rightarrow 2p$ emission (see Fig. S3). In order to estimate the probability for these (and related) nonlinear x-ray optical effects, we follow the formalism proposed in ref. (51) of the main text. Combining equations (8) to (10) from that reference, we obtain the atomic x-ray optical transparency due to (x-ray optical nonlinear) stimulated emission

$$T_{NL}^{atom} = 1 - \sigma_{abs}^{NL}/\sigma_{abs} = 2\tilde{\rho}_{22}(\infty) \qquad (19)$$

where the atomic absorption cross section σ_{abs}^{NL} is reduced with respect to σ_{abs}, the cross section unaffected by these effects. $\tilde{\rho}_{22}(\infty)$ is the effective excited state population, adopted from equation (9) in ref. (51) of the main text. According to this reference, the term is expressed as

$$\tilde{\rho}_{22}(\infty) = \frac{I_0 \Gamma_x \xi_{\mathrm{coh}} {\lambda_0}^3/(8\pi^2 c)}{(\Gamma/2)^2 + I_0 \Gamma_x \xi_{\mathrm{coh}} {\lambda_0}^3/(4\pi^2 c)} \qquad (20)$$

with I_0 being the x-ray intensity (power per area), $\Gamma = 0.32$ eV is the life time width of the 2p core hole (ref. (13) of the main text), c is the speed of light, and $\lambda_0 = 1.94$ nm is the x-ray wave length at 640 eV photon energy. $\Gamma_x = 0.46$ meV is the dipole transition width on resonance, which for consistency is

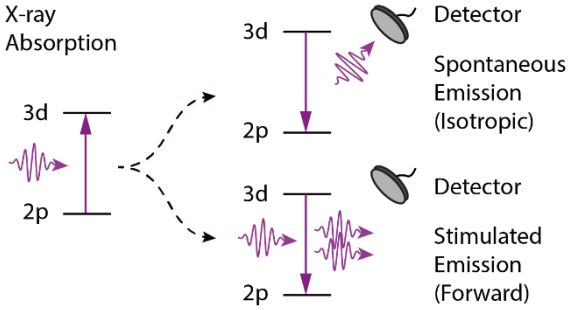

Fig. S3: Two competing processes subsequent to $2p \rightarrow 3d$ x-ray absorption. Top: The isotropic spontaneous $3d \rightarrow 2p$ emission is observed by a detector perpendicular to the beam axis. Bottom: The stimulated $3d \rightarrow 2p$ emission is directed along the x-ray beam axis and is not observed by the detector.

here deduced from the experimental cross section on the Mn L_3 peak resonance[4], $\sigma_{res}(\mathrm{Mn\ L_3}) \propto 12\ \mathrm{Mbarn} = 12 \times 10^{-22}$ m^2 via the relation $\sigma_x = 2\lambda f''_{res} = (\lambda_0^2 \Gamma_x)/(\Gamma\pi)$, where the theoretical resonant cross section σ_x=35 Mbarn is connected to the experimental cross section via an empirical factor $\sigma_x = 2.9 \times \sigma_{res}$. This factor of 2.9 accounts for the discrepancy of experimental and theoretical line shapes typically occurring for 3d metal L-edge XAS (ref. (51) of the main text). The term $\xi_{\mathrm{coh}} = \rho_a {\lambda_0}^2 d/4\pi$ is a coherent enhancement factor as a function of the x-ray wavelength λ_0, the Mn atom density $\rho_a = c \cdot N_A$ (Mn concentration c times Avogadro's number N_A) and the sample thickness d which for aqueous solutions is here approximated with the x-ray attenuation length $\mathrm{d} \approx \Lambda = 0.80$ µm of liquid water at 640 eV photon energy (1). The values obtained for $T_{NL} = T_{NL}^{atom}(I_0)$ are calculated for the peak intensity and the values $\bar{T}_{NL} = T_{NL}^{atom}(\bar{I}_s)$ are calculated for the skin volume averaged intensities $\bar{I}_s$ as listed in Table S5.

The averaged transparency values $\bar{T}_{NL}$ have magnitudes not noticeable within the experimental uncertainties of the relative PFY-XAS intensities. Experimentally, a comparison of the XFEL spectrum of 500 mM Mn^{2+}_{aq} solution in the main text to that measured at a stable synchrotron source (ref. (22) of the main text), shows no significant signal reduction of e.g. the most prominent Mn L_3 resonant peak in the XFEL spectrum (see Fig. S4). Hence no significant loss of PFY-XAS intensity to stimulated forward scattering is observed for the sample with the largest expected x-ray induced transparency, which strongly suggests the absence of stimulated emission and related nonlinear x-ray optical effects. Comparing the relative PFY-XAS spectral intensities of the synchrotron and the FEL spectra of Mn^{2+}_{aq} in Fig.S4, it should be noted that the respective deviations are on the order of magnitude of the experimental uncertainty of these relative intensities.

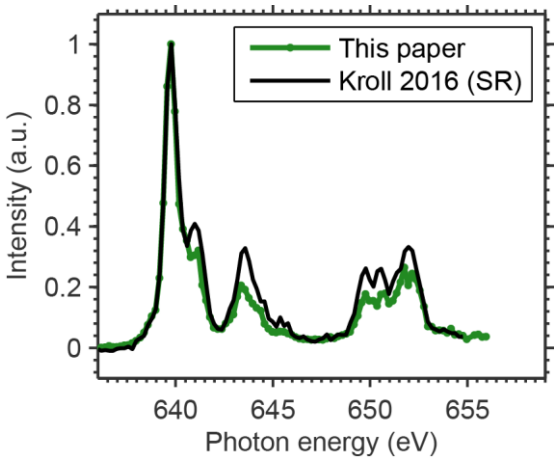

Fig. S4: Comparison of PFY-XAS spectra measured with the same setup on 500 mM Mn^{2+}_{aq} solution. The spectrum measured at the BESSY II synchrotron (black) was published previously in ref. (22) in the main text, the green curve is the XFEL spectrum shown in the main paper. Both spectra are normalized to their maximum intensity values.

[4] Personal communication by S. Schreck and Ph. Wernet, Helmholtz-Zentrum Berlin, Germany 2017.

References for the Supporting Information

1. Henke BL, Lee P, Tanaka TJ, Shimabukuro RL, & Fujikawa BK (1982) Low-energy x-ray interaction coefficients: Photoabsorption, scattering, and reflection. *Atomic Data and Nuclear Data Tables* 27(1):1-144.
2. Krause MO (1979) Atomic radiative and radiationless yields for K and L shells. *Journal of Physical and Chemical Reference Data* 8(2):307.
3. Rehanek JK (2014) Beam Diagnostics and Spectroscopy at X-ray Free Electron Lasers. (Freie Universität Berlin, 14195 Berlin, Germany).
4. Hau–Riege SP, Bionta RM, Ryutov DD, & Krzywinski J (2008) Measurement of x-ray free-electron-laser pulse energies by photoluminescence in nitrogen gas. *Journal of Applied Physics* 103(5):053306.
5. Tiedtke K*, et al.* (2008) Gas detectors for x-ray lasers. *Journal of Applied Physics* 103(9):094511.
6. Tiedtke K*, et al.* (2014) Absolute pulse energy measurements of soft x-rays at the Linac Coherent Light Source. *Opt Express* 22(18):21214-21226.
7. Moeller S*, et al.* (2015) Pulse energy measurement at the SXR instrument. *J Synchrotron Radiat* 22(3):606-611.